Kinetic Monte Carlo Simulation for Homogeneous Nucleation of Metal Nanoparticles during Vapor Phase Synthesis

Seyyed Ali Davari and Dibyendu Mukherjee

Dept. of Mechanical, Aerospace and Biomedical Engineering, Nano-BioMaterials Laboratory for Energy, Energetics & Environment (nbml-E^3), University of Tennessee, Knoxville, TN 37996

DOI 10.1002/aic.15887

Published online in Wiley Online Library (wileyonlinelibrary.com)

We present a free-energy driven kinetic Monte Carlo model to simulate homogeneous nucleation of metal nanoparticles (NPs) from vapor phase. The model accounts for monomer-cluster condensations, cluster–cluster collisions, and cluster evaporations simultaneously. Specifically, we investigate the homogeneous nucleation of Al NPs starting with different initial background temperatures. Our results indicate good agreement with earlier phenomenological studies using the Gibbs' free energy formulation from Classical Nucleation Theory (CNT). Furthermore, nucleation rates for various clusters are calculated through direct cluster observations. The steady-state nucleation rate estimated using two different approaches namely, the Yasuoka-Matsumoto (YM) and mean first passage time (MFPT) methods indicate excellent agreement with each other. Finally, our simulation results depict the expected increase in the entropy of mixing as clusters approach the nucleation barrier, followed by its subsequent drastic loss after the critical cluster formation resulting from first-order phase transitions. © 2017 American Institute of Chemical Engineers *AIChE J*, 00: 000–000, 2017

Keywords: homogeneous nucleation, Kinetic Monte Carlo, condensation, evaporation, Al nanoparticles

Introduction

Recent years have seen a rise in the use of metal nanoparticles (NPs) as novel energetic, catalytic, and semiconductor materials with engineered functionalities.[1,2] To this end, it becomes imperative to tune the structure-property characteristics of these NPs by tailoring their sizes and architectures during industrial or, laboratory-based vapor phase synthesis involving rapid cooling of saturated atoms or molecules (monomers). Particle formation from vapor phase occurs in two distinct stages: (1) homogeneous nucleation that produces thermodynamically stable condensed phase in the form of a critical nucleus within a metastable phase, and is the precursor to the crystallization process; (2) subsequent growth by coagulation and condensation/evaporation processes of the critical nucleus to NPs of larger sizes.

Homogeneous nucleation is a kinetically disfavored process that involves surmounting a nucleation barrier during the vapor phase cooling of monomers. The process leads to cluster growth via collisions and/or condensation of monomers, or cluster decomposition into smaller clusters and monomers via evaporation.[3,4] The processes continue until a critical nucleus is formed as a new phase perched atop the nucleation barrier. Any perturbation at this stage allows the critical nucleus to undergo barrier-less spontaneous growth. In the framework of classical nucleation theory (CNT), the Gibbs' free energy of a cluster formation with size i, ΔG_i^f, contain two terms; a favorable bulk free energy term and an unfavorable surface energy term due to the formation of an interface between the phases.[5–8] However, the presence of a free energy barrier in a first-order phase transition process makes nucleation a rare event. A few significant experimental efforts in the past have investigated the synthesis of nanoparticles via flame synthesis routes.[9–11] But, the exceedingly small length and time scales of the nucleation process pose significant challenge for designing experiments that can accurately monitor and control the in-situ NP formation.[12–14] It needs to be mentioned here that although CNT assumptions have been much debated over the years, a vast majority of homogeneous vapor phase nucleation studies resort to CNT due to its ability to predict relatively accurate results in a convenient fashion.[5,15–19] The main point of contention in CNT arises from the capillarity approximation that extends bulk thermodynamic properties to nano-scale clusters. This, in turn, leads to errors in the free energy estimation of clusters below the critical size.[20,21]

The aforementioned challenges highlight the need for hi-fidelity simulations that can model the mechanistic and collective picture of vapor-phase homogenous nucleation for predictive synthesis of tailored metal NPs. Past phenomenological models have resorted to solving population balance equations using sectional and nodal techniques[3,16] including our hybrid nodal method that accounted for size-dependent surface tension in the nucleation study.[22] Although such methods are robust and capture large time-scale processes, they suffer from numerical diffusion and round-off errors due to the discrete binning of cluster sizes, and resort to steady-state nucleation rate derivations in many cases. Conversely, molecular simulations comprising both Monte Carlo (MC) and molecular dynamics (MD) modeling have been used to estimate the

Correspondence concerning this article should be addressed to D. Mukherjee at dmukherj@utk.edu.

structural and free energy variations from first principles.[23] To this end, MC configuration integral and MD simulations enabled the calculation of Gibbs free energy changes and association rate constants for Al clusters.[7,24] Although such atomistic simulations capture the physics of NP formation at specific temperatures and saturation ratios, they fail to capture the ensemble nucleation process during real-time cooling of a background gas.[25] Specifically, this becomes computationally challenging bearing in mind that typical MD time scales (~1 fs) would require 10^{14} time-steps to simulate such a process. Conversely, MC has the ability to capture ensemble processes leading to rare events and is not being limited to MD time scales. However, unlike MD simulations, it is limited on its ability to capture the detailed atomistic picture of the process dynamically.

Here, we develop a stepwise constant-volume kinetic Monte Carlo (KMC) model to simulate vapor phase nucleation of Al NPs via random collisions and temporal evolution of clusters. We use the CNT-based formulation for Gibbs' free energy of cluster formation to allow for easy comparison with earlier nucleation studies.[3] The model is based on the fundamental principles of Metropolis algorithm and applies a pseudosampling technique that is capable of capturing the rarity of first-order phase transitions. To the best of our knowledge, no similar KMC models have been developed till date to simulate ensemble gas-to-particle conversions during rapid cooling of gas phase monomers without *a priori* constraints on the system cluster distributions.

Mathematical Model and Theory

The change in Gibbs' free energy of cluster formation (ΔG_i^f) comprising of i monomers (i.e., an i-mer) based on the self-consistent CNT is expressed as[26]

$$\frac{\Delta G_i^f}{k_B T} = \theta(i^{2/3}-1)-(i-1)\ln(S) \tag{1}$$

where θ is the dimensionless surface tension defined as

$$\theta = (36\pi)^{1/3} v_1^{2/3} \frac{\sigma}{k_B T} \tag{2}$$

and, v_1, σ, k_B, and T are volume of monomer, surface tension, Boltzmann constant and temperature respectively. S is the saturation ratio given as the ratio of monomer concentration in the simulation box (n_1) to the saturated monomer concentration (n_s) based on the saturated vapor pressure of monomers in equilibrium with its liquid phase at a specific T

$$S = \frac{n_1}{n_s} \tag{3}$$

Figure 1 illustrates ΔG_i^f as a function of cluster size. Based on the Gibbs free energy of formation, the equilibrium size distribution can be expressed as

$$n_i^e = n_1 \exp\left(-\frac{\Delta G_i^f}{k_B T}\right) \tag{4}$$

The size distribution of clusters that undergo cluster–cluster collision, condensation and evaporation is given by the population balance equation

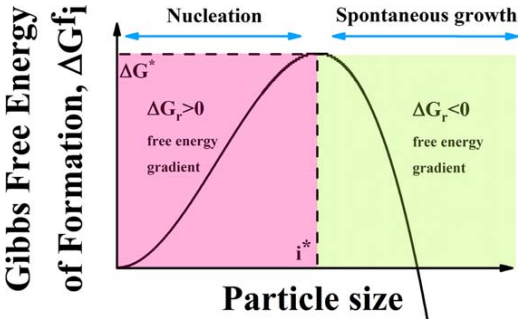

Figure 1. Gibbs free energy of cluster formation (ΔG_i^f) as a function of particle size.

The left side of the barrier ($\Delta G_i^f < \Delta G^*$) corresponds to nucleation process, and the right side of the barrier ($\Delta G_i^f > \Delta G^*$) corresponds to surface growth and coagulation. [Color figure can be viewed at wileyonlinelibrary.com]

$$\frac{dn_i}{dt} = \frac{1}{2}\sum_{j+k=i} K_{j,k} n_j n_k - n_i \sum_{j=2} K_{j,i} n_j + (k_{f,(1,i-1)} n_{i-1} n_1 - k_{b,(i)} n_i) - (k_{f,(1,i)} n_i n_1 - k_{b,(i+1)} n_{i+1}) \tag{5}$$

where n_i is the concentration of i-mer particles and $K_{i,j}$ is the free molecular collision kernel between an i-mer and j-mer

$$K_{i,j} = \left(\frac{3v_1}{4\pi}\right)^{1/6} \left(\frac{6k_B T}{\rho}\right)^{1/2} \left(\frac{1}{i}+\frac{1}{j}\right)^{1/2} (i^{1/3}+j^{1/3})^2 \tag{6}$$

where ρ is the mean density of clusters. In Eq. 5 $k_{f,(1,i-1)}$ is the forward reaction rate between a (i-1)-mer and a monomer and $k_{b,(i)}$ is the backward reaction rate for the dissociation of an i-mer. These forward and backward rates are associated with the following reaction

$$A + A_{i-1} \underset{k_{b,(i)}}{\overset{k_{f,(1,i-1)}}{\rightleftharpoons}} A_i \tag{R1}$$

From Eq. 1, the difference in Gibbs free energy during (R1) is given as

$$\frac{\Delta G_{i,i-1}^r}{k_B T} = \frac{\Delta G_i^f}{k_B T} - \frac{\Delta G_{i-1}^f}{k_B T} = \theta[i^{2/3}-(i-1)^{2/3}] - \ln(S) \tag{7}$$

Furthermore, thermodynamic equilibrium constants are defined as

$$K_p = e^{\frac{-\Delta G_{i,i-1}^r}{k_B T}} \tag{8}$$

$$K_c = \frac{k_{f,(1,i-1)}}{k_{b,(i)}} \tag{9}$$

$$K_p = K_c n_1 \tag{10}$$

Hence, based on Eqs. 8–10, the backward reaction rate can be derived as[27]

$$k_{b,(i)} = k_{f,(1,i-1)} n_s \exp\left(\theta[i^{2/3}-(i-1)^{2/3}]\right) \tag{11}$$

where $k_{f,(1,i-1)}$ is assumed to be the free molecular collision kernel $K_{i-1,1}$ between clusters with sizes i-1 and monomers.

KMC Model Development

Numerous studies have investigated the evolution of aerosol size distributions using MC methods[28–37] that have shown the capabilities of MC approach to approximate aerosol growth processes. Generally, MC methods can be divided into two classes: Constant-Volume (*Constant-V*) and Constant-Number (*Constant-N*). In the *Constant-V* method, the number of particles in the system reduces over time. Due to the accuracy of MC simulations being proportional to $\frac{1}{\sqrt{N}}$,[38] this method is only applicable to systems with large number of particles and hence, is computationally expensive. To overcome this, two different MC methods have been classically proposed. The first is the Constant-N method which the number of system particles is kept fixed by adding a particle at each time step. And the second is the stepwise constant-V[39] method wherein the system duplicates the particles array whenever the number of particles drops to half of the initial value.[38]

The aforementioned stepwise constant-V MC via duplication can be implemented in two directions. In the first approach (time-driven), a time step is chosen and the number of events is specified by the probability of events driven by MC. In the second approach (event-driven), an event is identified through the MC and an appropriate time increment is calculated and added to the time.[29] The advantage of the latter is that one does not need to specify any precalculated time increment prior to the simulation. However, the rates of transition between the states are required in both the cases.

Based on our earlier KMC model[40], this study uses the stepwise constant-V method in conjunction with the event-driven approach to simulate the vapor phase nucleation of Al NPs. First, we identify an event based on the MC probability of success for the event. Then, driven by the transition rate for the selected event, a time increment is calculated and added to the MC time scale. Assigned probabilities are derived based on the Gibbs free energy change associated with (R1) and the free molecular collision kernel given by Eq. 6. All simulations presented here start with 20,000 monomers in the MC volume.

Implementing the MC Algorithm

At each MC time step, two processes can take place namely, growth (categorized as condensation and cluster-cluster collisions), and/or evaporation. By condensation, we refer to collisions between a monomer and *i*-mer, whereas cluster-cluster collisions indicate collisions between an *i*-mer and a *j*-mer. Each of these processes has inherent MC probabilities assigned to them. Using a random number generator, two clusters with sizes *i* and *j* are first chosen *(i, j* $\in [1, M]$, where M is the total number of MC clusters). Based on the condensation or cluster–cluster collision probabilities, two clusters with sizes *i* and *j* might be combined to form a new cluster with size $i + j$, and the total number of clusters is reduced by unity. Furthermore, a cluster with size k is randomly chosen such that $k \in [2, M]$. Based on the evaporation probability, the cluster with size k is decomposed to a cluster with size k-1 and a monomer, and the total number of monomers is increased by unity. Any statistical inaccuracies arising from cluster depletion are addressed by duplicating the system when the total number of clusters in the system drops to half of the initial value. Such topping-up does not change the cluster size distribution owing to periodic boundary conditions, while conserving the system mass loading due to corresponding adjustments in the MC volume.

Cluster-Cluster Collision

Cluster–cluster collision occurs when an *i*-mer and a *j*-mer collide. The probability of the collision event ($P_{\text{collision}}$) is determined from the free molecular collision kernel as[40]

$$P_{\text{collision}} = \frac{K_{i,j}}{K_{\max}} \tag{12}$$

where $K_{\max}$ is the maximum value of the kernel among all clusters. Mathematically, it can be inferred that the maximum kernel occurs when $i = 1$ and $j = i_{\max}$ where $i_{\max}$ is the maximum cluster size in the system. Theoretically in Eq. 12, $K_{i,j}$ should be normalized by the sum of all kernels. However, normalizing to $K_{\max}$ makes the computational cost less intensive without affecting the accuracy noticeably.[41–43]

Condensation

Condensation refers to collisions between a monomer and an *i*-mer. Based on the Metropolis algorithm, the probability of condensation is defined as

$$P_c = \begin{cases} e^{\frac{-\Delta G^r_{i,i-1}}{k_B T}} & \Delta G^r_{i,i-1} > 0 \\ 1 & \Delta G^r_{i,i-1} > 0 \end{cases} \tag{13}$$

Equation 13 states that the transition probability between this state and the trial state has a Boltzmann distribution. It can be realized from Figure 1 that the difference in Gibbs free energy during (R1), and as expressed by Eq. 7, is always positive for the clusters smaller than the critical cluster ($\Delta G^r_{i,i-1} > 0$), and is negative for the clusters/particles larger than the critical cluster ($\Delta G^r_{i,i-1} < 0$), where the critical cluster size is denoted as i^*.

After the nucleation burst, a barrier-less condensation on critical clusters will result in spontaneous particle growth with a probability of unity ($P_c = 1$) as seen from Eq. 13. However, now the driving force for monomer condensation on a particle is the difference between n_1 and the saturated monomer concentration (or the saturated vapor pressure) on an *i*-mer ($n_{s,i}$) droplet. Hence, based on the reaction rate for condensation driven by Kelvin relations, the probability of surface growth ($P_{\text{surf growth}}$) after the nucleation burst (for $i > i^*$) is modeled as

$$P_{\text{surf growth}} = \frac{K_{1,i\,1}}{K_{\max}} \left(1 - \frac{n_{s,i\,1}}{n_1}\right) \tag{14}$$

where, $n_{s,i}$ over an *i*-mer is obtained from the Kelvin relations as

$$n_{s,i} = n_s \exp\left(\frac{4\sigma v_1}{d_i k_B T}\right) \tag{15}$$

where, d_i is the diameter of an *i*-mer.

Evaporation

The probability of evaporation (P_e) for reaction (R1) is derived from the probability of condensation (P_c) using detailed balancing as

$$P_e = \begin{cases} 1 & \Delta G^r_{i,i-1} > 0 \\ e^{\frac{\Delta G^r_{i,i-1}}{k_B T}} & \Delta G^r_{i,i-1} > 0 \end{cases} \tag{16}$$

Equation 16 indicates that for the left side of the nucleation barrier (where $\Delta G^r_{i-1,i} = -\Delta G^r_{i,i-1} \leq 0$), evaporation always

happens successfully. However, for the right side of the nucleation barrier (where $\Delta G^r_{i-1,i} = -\Delta G^r_{i,i-1} > 0$), evaporation should be restricted by the Boltzmann factor. However, as also explained earlier, the evaporation of particles during the relaxation after the nucleation burst is also driven by the relative difference between n_1 and $n_{s,i}$. Hence, driven by the Kelvin relations (as explained earlier), the probability of evaporations after the nucleation burst (P_{diss}) (for $i > i^*$) is modeled as

$$P_{diss} = \frac{K_{1,i}}{K_{\max}} \left(1 - \frac{n_1}{n_{s,i}}\right) \tag{17}$$

KMC Time Step

For the growth processes, the KMC time is inversely proportional to the sum of the rates of all possible growth events as

$$\Delta T_f = \frac{V}{\sum R} = \frac{2V}{\sum_{i=1}^{M} \sum_{j=1, j\neq i}^{M} K_{i,j}} \tag{18}$$

where V is the MC volume calculated from the initial monomer concentration and number of clusters ($V = \frac{M_0}{n_0}$). Considering the stochastic equilibrium for the KMC system, the summation in Eq. 18 is estimated from the collision kernel of the selected pair for the sake of computational efficiency[33,42,44]

$$\Delta T_f \approx \frac{2V}{M(M-1)K_{ij}} \tag{19}$$

where K_{ij} is the collision kernel of the selected pair.

Moreover, from Eq. 11 the MC time step for evaporation events can be calculated from

$$\Delta T_b = \frac{1}{\sum k_b} \approx \frac{1}{K_{1,i-1} e^{\theta[i^{2/3} - (i-1)^{2/3}]} n_s M} \tag{20}$$

Thus, the final MC time step is given by

$$\Delta T = \frac{1}{\frac{1}{\Delta T_f} + \frac{1}{\Delta T_b}} \tag{21}$$

Nucleation: A Rare Event

Nucleation is a rare event that is difficult to capture numerically through direct brute force simulations.[45] For the condensation, it can be easily realized from the P_c distribution in Figure 2 that larger clusters have higher probabilities of being sampled than smaller ones in the system. To avoid this stochastic bias towards the larger clusters in condensation events, one needs to account for their relatively lower concentrations in the system during the growth process. Thus, a cluster needs to have a relatively high probability (P_c) as well as concentration to grow successfully. To overcome such issues in our MC system, we define the probability of choosing a cluster size as

$$P_{\text{choose}} = \frac{N_i}{M} \tag{22}$$

where N_i is the number of clusters with size i in the simulation box and M is the total number of clusters in the MC. Figure 2 depicts the distributions of P_c and P_{choose} assuming equilibrium cluster distributions. For any particular temperature and saturation ratio, P_c increases and P_{choose} decreases with

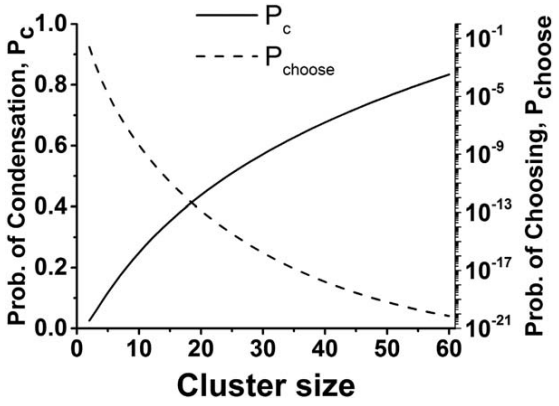

Figure 2. The probabilities of condensation (P_c) and choosing (P_{choose}) as a function of cluster sizes as obtained from the Boltzmann equilibrium distributions.

increasing cluster sizes in the system. As an example, the relatively elevated concentrations of monomers result in them exhibiting the minimum values for P_c and maximum values for P_{choose} in the system. Conversely, the maximum cluster sizes ($i_{\max}$) in the system have the lowest P_{choose}, alone with highly elevated values for P_c. To account for the role of P_{choose} in our KMC model, we employ the following sampling scheme for condensation events.

Sampling Scheme

The sampling scheme is implemented in two steps: (1) identifying a "possible trial" and (2) comparing it to the "best trial." Identification of a "possible trial" is performed by randomly choosing two clusters, and then deciding on the success of the event by comparing its condensation probability (P_c) to a random number. If P_c is larger than the chosen random number ($P_c \geq \Re \in [0, 1]$), it is considered as a "possible trial" move. Otherwise, the system searches for another possible trial. To determine the "best trial" move, all existing growth paths in the system are considered and their probabilities of condensation (P_c) are calculated. Then, the probability of each path is compared to a random number ($\Re$) to determine the paths that satisfy $P_c \geq \Re \in [0, 1]$. Among these paths, the path with the greatest P_c is identified as the "best trial" candidate. This random procedure for selecting the "best trial" ensures unbiased sampling in the system. Finally, we require the product of P_c and P_{choose} for the "possible trial" $(P_{\text{choose}} \cdot P_c)^{\text{possible}}$ to be larger than the corresponding probability product for the "best trial" $(P_{\text{choose}} \cdot P_c)^{\text{best}}$ in the system for a successful growth to proceed, that is

$$(P_{\text{choose}} \cdot P_c)^{\text{best}} \leq (P_{\text{choose}} \cdot P_c)^{\text{possible}} \tag{23}$$

The algorithm flowchart and a schematic representation of the sampling technique are demonstrated in a step-wise fashion in Figures 3 and 4, respectively. This strategy ensures that the acceptance of the growth reaction is not only based on the probability of condensation but also on the probability of choosing (driven by cluster concentrations). As also described earlier, the probability criteria for backward evaporation processes are accordingly derived from detailed balancing.

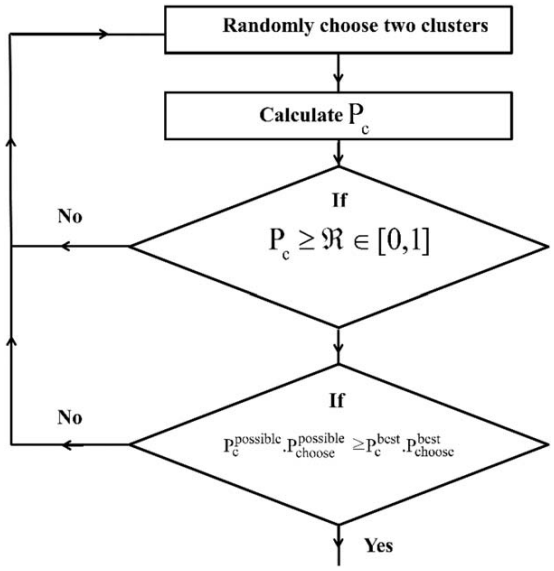

Figure 3. Schematic showing the algorithm for the pseudosampling technique adopted for the current KMC model.

Results and Discussion

This KMC model specifically studies the vapor phase nucleation of Al NPs. The choice of Al NP stems from the growing interest in diverse applications of Al nanomaterials in semiconductors,[46] nanocomposites,[47,48] and specifically, in energetic nanomaterials for solid-state combustion studies carried out by numerous earlier experiments[1,49–52] and simulations.[43,53–56] Table 1 shows the thermophysical properties of Al used for the simulations. The choice of Al NPs also enables the model validation via comparisons with previous phenomenological studies using Nodal General Dynamic Equation (NGDE) model[3,25] under identical synthesis conditions (indicated as case (a) below). Additionally, we implement the model to simulate the process under two different initial conditions as depicted by cases (a) and (b) below. Simulation jobs were run at the Newton cluster machines operated by the University of Tennessee. The machine consists of over 300 Linux compute nodes, 4200 × 86_64 architecture processors, and 8000 Gbytes of RAM with 48 of the compute nodes featuring Tesla GPU compute accelerators. Typical CPU run time for jobs run on one node with 10000 particles is ~2 h, that can slightly change based on the type of processor that the machine decides to assign the job to. The following synthesis parameters are chosen for the simulation results presented in this study:

a. Initial temperature, $T_0 = 1773$K and cooling rate = 1000K/s.
b. Initial temperature, $T_0 = 1973$K and cooling rate = 1000K/s.

Model verification

The temporal evolution of ΔG_i^f as a function of cluster size is plotted for the representative case (a) in Figure 5. Initially, the saturation ratio in the system is approximately one (S~1). As seen from Figure 5, the initial nucleation barrier, as calculated from the CNT expression (Eq. 1), is extremely elevated. Thus, the chance of clusters surmounting this barrier is significantly low. The nucleation barrier reduces over time as the background temperature (T) decreases and the saturation ratio (S) increases.

To verify the model, the temporal evolution of S and monomer concentrations (n_1, #/m^3) from the current KMC simulations, as depicted in Figures 6A, B respectively, indicate good agreement with the corresponding results from previous NGDE simulations.[3] Due to high cluster evaporation rates in early stages, the KMC monomer concentration demonstrates a uniform and slow decay until the point of nucleation (Figure 6B).

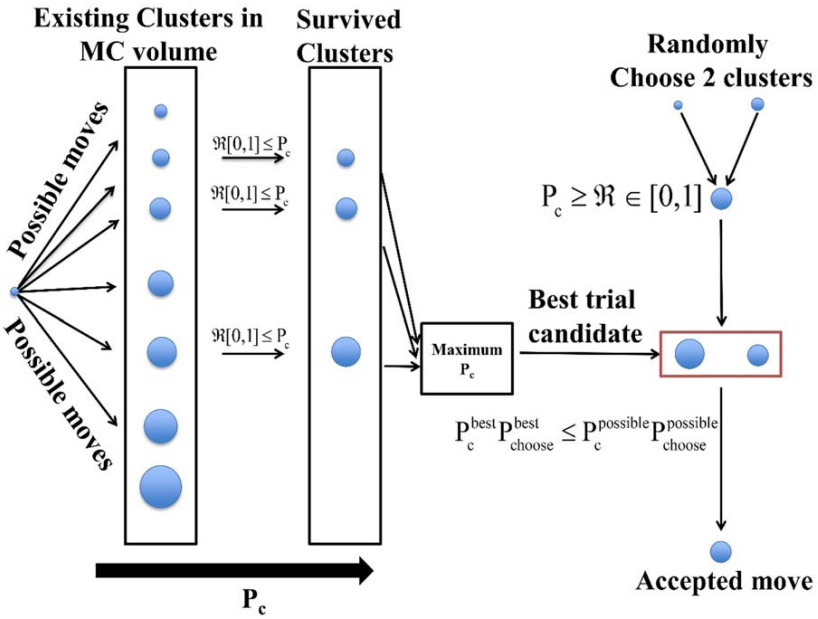

Figure 4. Schematic showing the pseudosampling technique used to capture the rare nucleation event in the KMC model without any stochastic bias.

[Color figure can be viewed at wileyonlinelibrary.com]

Table 1. Thermophysical Properties of Aluminum

Properties	Value
Density, ρ [kg/m^3]	2700
Atomic mass unit, m [u]	27
Monomer volume, V_1 [m^3]	1.657×10^{-29}
Saturation vapor pressure, P_s [Pa]	$\exp(13.07 - \frac{36373}{T}) P_g$ [a]
Surface tension, σ [N/m]	$(948 - (0.202 \times T_g) \times 10^{-3}$

[a] P_g: Pressure of gas medium [Pa].

This also corresponds to a steady increase in the saturation ratio from S∼1 to S∼5.4 at the onset of nucleation (t∼0.145 s). A negative Gibbs' free energy change for the evaporation reactions before the onset of nucleation ($\Delta G^r_{i,i-1} \leq 0$) results in the maximum evaporation probability ($P_e = 1$ from Eq. 16). Thus, a majority of the generated clusters undergo enhanced evaporation leading to low cluster concentrations and minimal decay in monomer concentrations. Figures 6A, B show a drastic drop in S and n_1, respectively, at the onset of nucleation. This can be explained by the formation of a critical cluster with size i^* as a new phase. The birth of the critical clusters initiates rapid consumption of monomers by condensation, and surface growth that leads to the formation of larger particles. Subsequently, the supersaturated vapor relaxes back to the saturated state (S∼1) as the monomer vapor pressure equilibrates with the saturated vapor pressure on surfaces of the formed particle (Figure 6A). It can be observed that the relaxation of S form the KMC model is slightly different as compared to that from NGDE. This can be related to the numerical diffusion involved in NGDE, especially when the nucleation outburst occurs and larger bins start to get occupied.

The plots for P_{choose} and P_c as a function of cluster size in Figure 7 for case (a) at $t = 0.111$, 0.126, and 0.14 s indicate the inverse relations of P_c and P_{choose} with increasing cluster sizes which is characteristic of rare events. The qualitative trends in these characteristic variations have been corroborated earlier for theoretical P_{choose} and P_c values in Figure 2 under equilibrium size distribution considerations. This further supports our rationale behind the choice of P_{choose} as an additional parameter in the sampling technique described earlier in the modeling section to account for the rarity of the nucleation event. In addition, higher S and lower T may result in the appearance of larger clusters with higher surface areas. This, in the presence of excess monomer concentrations, increases

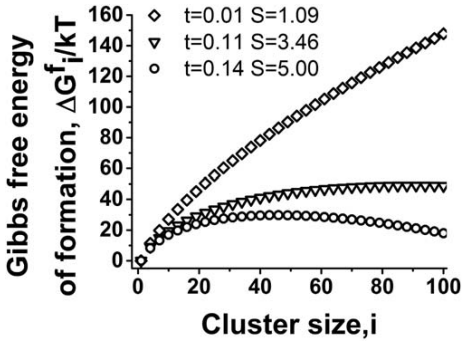

Figure 5. Temporal variation of normalized Gibbs free energy of formation $\left(\frac{\Delta G^f_i}{k_B T}\right)$ with cluster sizes (i) for T_0=1773 K indicating that the nucleation barrier decreases with time.

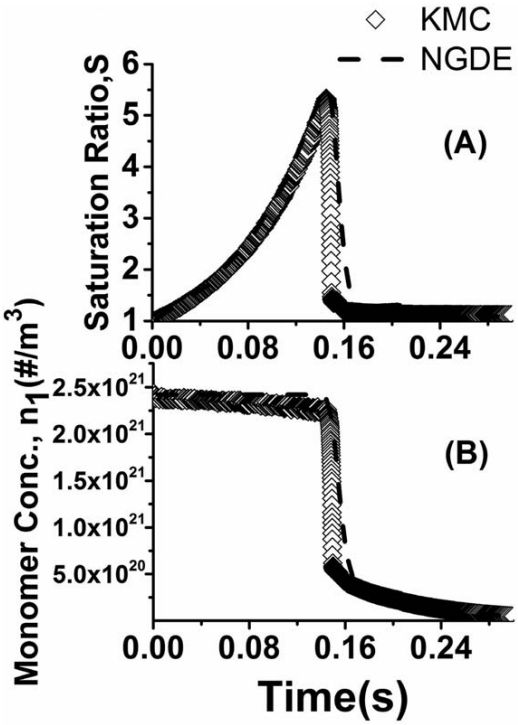

Figure 6. Temporal variation of (A) saturation ratio (S) and (B) monomer concentration n_1 (#/m^3) for T_0=1773 K case.

the likelihood of monomer condensation on clusters significantly. As the cluster sizes increase, the favorable bulk free energy difference due to chemical potential changes arising from phase transitions dominate over the unfavorable

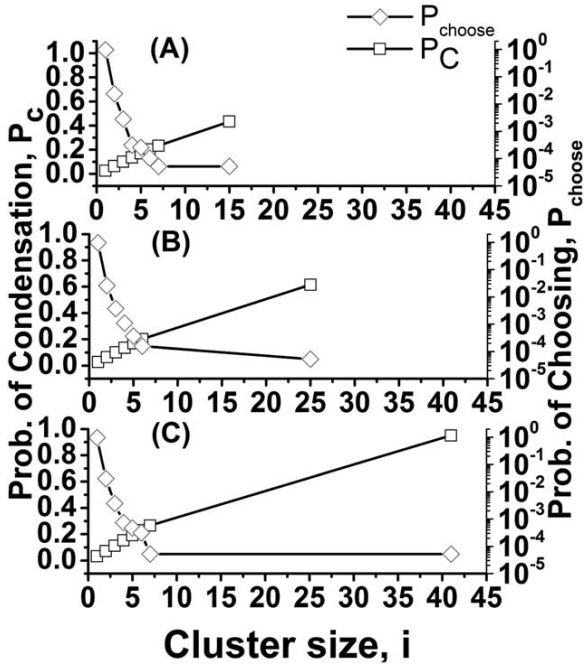

Figure 7. Probability of condensation (P_c) and choosing (P_{choose}) for T_0=1773K at (A) $t = 0.111$s, (B) $t = 0.126$s, and (C) $t = 0.14$s.

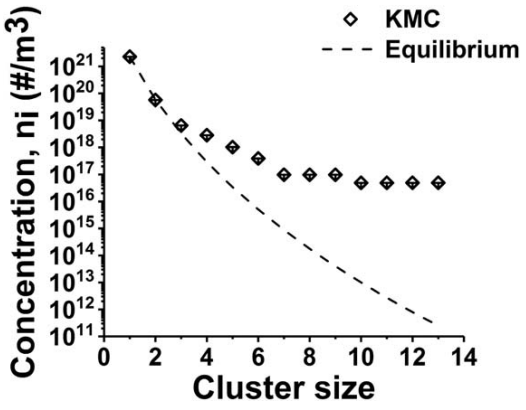

Figure 8. Cluster size distribution for $i<15$ indicating deviation from equilibrium size distributions for $T_0=1773$K at $t=0.11$ s.

formation of an interface between the phases. Thus, the forward rates of the reaction $R(1)$ is enhanced as the cluster sizes increase in the system. This phenomenon can be observed in Figure 7 where the P_c values increase rapidly as the cluster sizes in the system increase between $t=0.111$ s and $t=0.14$ s.

Despite the qualitative similarities between the variations of P_c and P_{choose} in Figures 2 and 7, a distinct quantitative difference is observed in the P_{choose} values for the larger clusters. The P_{choose} variations obtained from the KMC simulations (Figure 7) shows a well-defined plateau for larger cluster sizes as compared to the uniformly exponential decay in the equilibrium size distribution in Figure 2. Hence, Figure 8 compares the cluster concentration distributions for sizes $i<15$ based on KMC simulations for case (a) at $t=0.111$s with the corresponding equilibrium concentration distributions as depicted by Eq. 4 earlier. The comparison indicates that the deviations from equilibrium conditions are initiated as early as cluster sizes ranging between $i=4$–8. Such observations indicate that while equilibrium size distributions can approximately predict the concentrations of smaller clusters, the prediction fails drastically for larger clusters. These larger clusters, ultimately, play a primary role in formation of critical clusters when the process approaches the onset of nucleation burst. Similar results have also been observed in cluster size distributions from MD simulations,[57,58] as discussed extensively in the following section.

Nucleation rate: a discussion

The nucleation rate for cluster size of i (J_i) is defined as the net rate of transition from size i to the next size ($i+1$). To calculate the nucleation rates from our current KMC simulations, we use two different methods commonly adopted in earlier MD simulations: (1) Yasuoka-Matsumoto (YM) method, and (2) mean first passage time (MFPT) method.

Yasuoka-matsumoto method

This method, introduced by Yasuoka et al.,[57] was implemented in their MD simulations on Lennard-Jones fluid. In that study, the numbers of clusters equal or above a certain size threshold were counted and nucleation rates were estimated based on the slopes of the number of counts over time. Figures 9A, B illustrate the nucleation rates $<J_i>$ for various cluster sizes ($i=2,3,5$ in (A) and $i=10$, 15, 20 in (B)) as a function of time generated from our KMC simulations based on the YM method. Two distinct stages, S1 and S2 can be observed as it was also shown by Yasuoka et al.'s work. It is

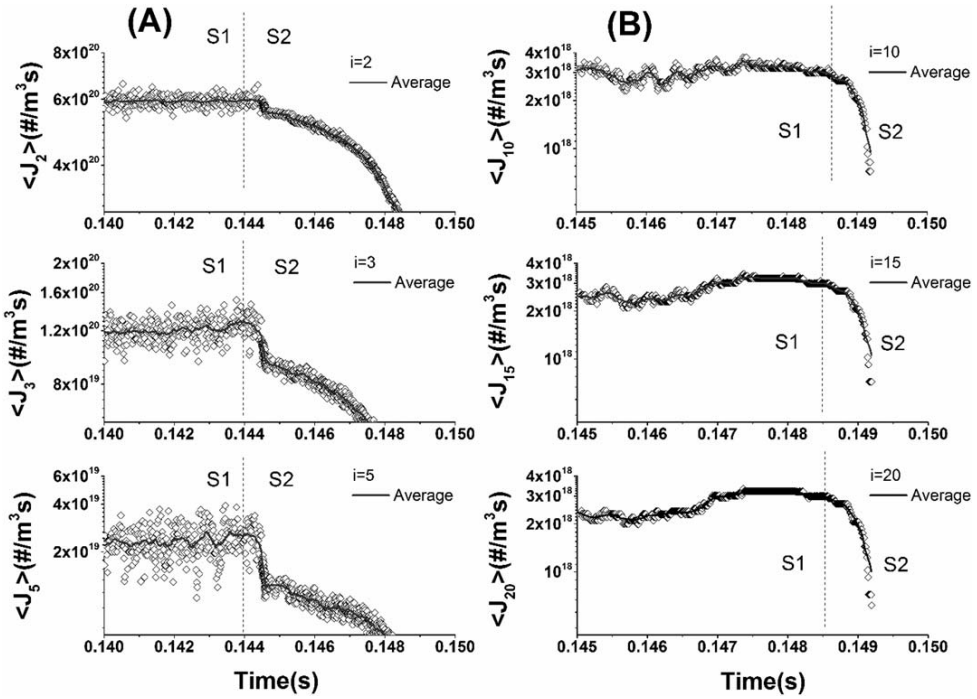

Figure 9. Nucleation rates $<J_i>$ for cluster sizes (A) $i=2$, 3, 5 and (B) $i=10$, 15, 20 as a function of time for $T_0=1773$K.

In the first stage (S1), nucleation rates are approximately constant, while in the second stage (S2), generation of new nuclei stops.

evident from Figure 9A that the $<J_i>$ for $i = 2$–5 indicate relatively high values that diminish with increasing cluster sizes (i.e., $<J_2> \sim 5.9 \times 10^{20}$ #/m^3.s and $<J_5> \sim 2.5 \times 10^{19}$ #/m^3.s) in stage S1 up to t $\sim$ 0.144 s. Additionally, the $<J_i>$ values decay rapidly in stage S2 beyond $t = 0.144$–0.145 s. In contrast, the $<J_i>$ for cluster sizes $i = 10$–20 in Figure 9B show lower values than those observed for $i = 2$–5, while no significant change in nucleation rates is observed for the increasing cluster sizes. The $<J_i>$ values decay rapidly beyond $t \sim$ 0.1485–0.149 s in stage S2, that also marks the onset of nucleation. It suggests that although in stage S1 significant numbers of clusters are formed with sizes smaller than the threshold value ($i < 10$), only clusters larger than the threshold value ($i \geq 10$) are able to grow through this stage and up to the nucleation outburst. To provide a detailed insight, Figure 10 shows that nucleation rates for smaller clusters ($i = 2$–9) are significantly higher than those for the larger ones ($i \geq 10$), and they decay to a lower but unified value for the larger clusters. Therefore, the KMC-based nucleation rate for cluster sizes ≥ 10 are estimated to be $J_{KMC} = 2.7 \times 10^{18}$ (#/m^3.s). Comparing this result to the theoretical CNT-derived value of $J_{CNT} = 1.81 \times 10^{14}$ (#/m^3.s), we observe almost four orders of magnitude differences between the two nucleation rates.

Mean First Passage Time Method (MFPT)

Mean first passage time method has been extensively studied in literature for calculating nucleation rates.[45,59–61] The method analyzes the time required for a cluster to reach to a particular size for the first time. By tracking the maximum cluster size of the system over time the nucleation rate can be obtained. It has been shown that in presence of nucleation barrier, the required time for maximum cluster size to reach a particular size is given by[45,59]

$$\tau(i) = \frac{\tau_J}{2}\left[1 + \mathrm{erf}(b(i - i^*))\right] \tag{24}$$

where "erf" represents error function, and b is related to the Zeldovich factor: $Z = \frac{b}{\sqrt{\pi}}$. Using a curve fit to the direct simulation results, it is possible to obtain critical cluster size and nucleation time. Finally, the nucleation rate can be calculated as

$$J_{KMC} = \frac{1}{V\tau_J} \tag{25}$$

where τ_J is obtained from curve fit and V is the MC volume. Figure 11 shows the MFPT curve obtained from tracking the evolution of maximum cluster size in our KMC system run for the case study (a). It can be observed that the data has a sigmoidal shape and represents a well-defined plateau. Therefore, the nucleation rate obtained from MFPT is estimated to be $J_{KMC} = 3.7 \times 10^{18} \pm 3.8 \times 10^{16}$. From Eq. 25 it can be realized that the nucleation rate depends on the nucleation time (τ_J) and the error is calculated based on the error in the nucleation time. By comparison, there is a good agreement between the nucleation rates obtained by YM and MFPT methods.

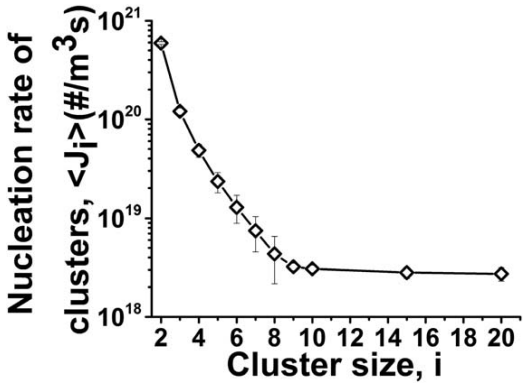

Figure 10. Nucleation rates $<J_i>$ (#/m^3.s) averaged over stage S1 as a function of cluster sizes for T_0=1773K.

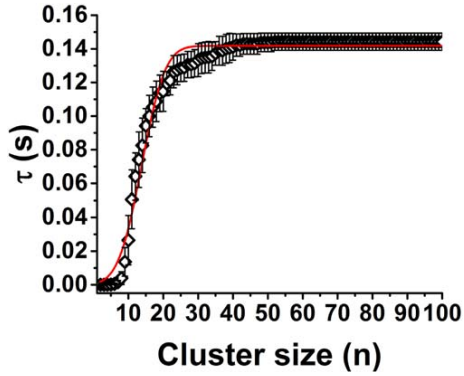

Figure 11. Mean first passage time analysis and curve fit for case (a).

[Color figure can be viewed at wileyonlinelibrary.com]

Effect of Initial Temperature

The KMC model is used to investigate the effect of initial background temperature on the nucleation process for two different values: $T_0 = 1773$ and 1973 K. Figure 12 shows the evolution of saturation ratios as a function of reduced temperature (defined as the instantaneous system temperature T normalized by the initial temperature T_0). As the T_0 values for the nucleating system are increased, the nucleation process is accelerated. Thus, the maximum saturation ratio is decreased from $S = 5.4$ in case (a) to $S = 2.7$ in case (b) and subsequently earlier onset of nucleation is resulted. Figure 13 shows the critical cluster sizes of $i^* = 43$ ($\sim$1 nm) for case (a) as compared to $i^* = 105$ ($\sim$ 2 nm) for case (b). Thus, a reduction of the initial system temperature assists in the formation of smaller primary particles. Furthermore, larger fluctuations in the i_{max} values are also observed for higher initial temperature in case (b) (i.e., $T_0 = 1973$ K in Figure 13A). Analyzing these fluctuations,

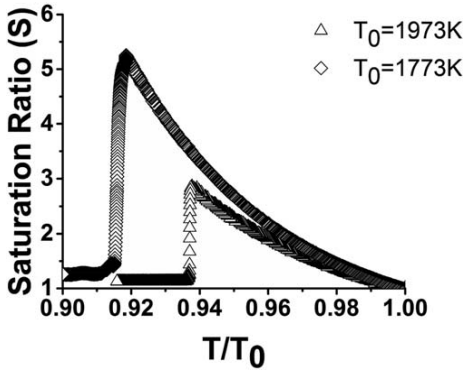

Figure 12. Saturation ratio (S) as a function of reduced temperature (T/T_0) for $T_0 = 1773$ K and 1973 K.

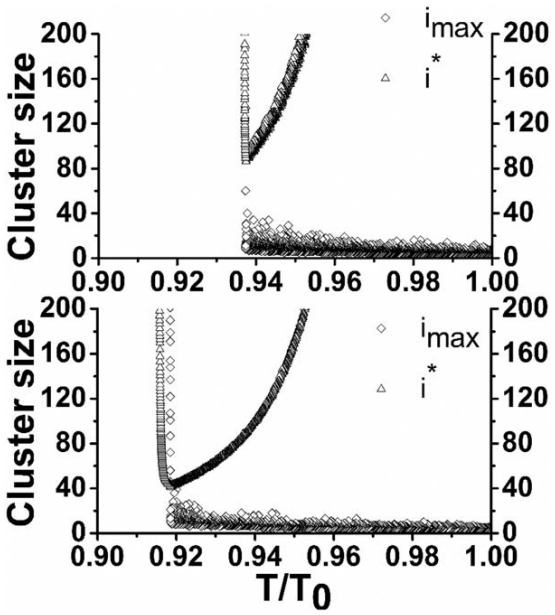

Figure 13. Variation of maximum cluster (i_{max}) and critical cluster size (i^*) in the system as a function of reduced temperature (T/T_0) for (A) $T_0 = 1973$ K, and (B) $T_0 = 1773$ K.

Figure 13A for $T_0 = 1973$ K shows a wide and uniform variance over time, as compared to Figure 13B for $T_0 = 1773$ K where the variance is initially narrow for $T/T_0 \sim 1$ but increases over time demonstrating a nonuniform trend. This implies that for $T_0 = 1973$ K, the i_{max} in the system can attain larger values in the earlier stages as compared to the corresponding i_{max} values for $T_0 = 1773$ K case. Moreover, for higher T_0 values the maximum cluster size in the system has a higher probability to grow and survive in spite of the high evaporation rates. To analyze these fluctuations in the nucleating systems, the Gibbs' entropy of mixing is calculated based on the probability distribution over cluster sizes as

$$\mathscr{S} = -k_B M \sum_{i=1}^{i=i_{max}} \frac{N_i}{M} \ln\left(\frac{N_i}{M}\right) = -k_B M \sum_i P_{choose} \ln(P_{choose}) \tag{26}$$

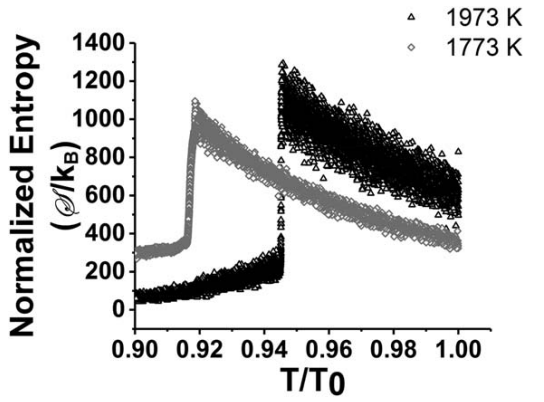

Figure 14. The evolution of normalized entropy ($\mathscr{S}/k_B$) as a function of reduced temperature (T/T_0) for $T_0 = 1773$ K and $T_0 = 1973$ K.

For further clarification, Eq. 26 represents the system entropy of mixing where different cluster sizes are considered as independent entities, and clusters within each size are identical. At each time step, the state of the system is determined by the cluster size distributions and the corresponding system temperature. Appearance of other cluster sizes increases the disorder, and consequently the entropy of mixing in the system. Clusters that cross the nucleation barrier form a more organized phase and hence, the entropy of mixing in the system should ideally decrease. These phenomena are clearly depicted by Figure 14 where the entropies for case (a) ($T_0 = 1773$ K) and case (b) ($T_0 = 1973$ K) are plotted as a function of the reduced temperatures (T/T_0). As expected, the higher entropy of mixing along with the large variabilities and spread in the entropy data as seen in case (b) indicate higher disorder and fluctuations in the system as compared to the case (a). These disorders and fluctuations cause a number of larger clusters to survive during the cluster evaporation that go on to attain the critical cluster size by crossing the nucleation barrier and initiating the nucleation process. A comparison of the cases (a) and (b) in Figure 14 reveals that higher fluctuations in case (b) result in an earlier outburst of nucleation.

Conclusion

We have developed a hi-fidelity Gibbs' free energy driven KMC model to simulate homogeneous nucleation of metal NP's. The model captures the ensemble stochastic processes of monomer-cluster (condensation), cluster–cluster collisions, as well as cluster evaporations via detailed balancing during gas phase synthesis process. A novel and statistically unbiased pseudosampling technique has been proposed to effectively address the computational challenges of capturing the rare and nonequilibrium nature of nucleation events in a time-efficient manner. The simulation results from the current KMC model indicate good agreement with previously obtained results from phenomenological models for similar case-studies.[3,25] Our results indicated that the onset of nucleation outburst is accelerated by increasing the initial vapor temperature (T_0) resulting in the formation of critical clusters with sizes $\sim$ 1 and 2 nm for $T_0 = 1773$ and 1973 K, respectively.

Nucleation rates calculated by the YM method indicate higher values for cluster sizes smaller than a threshold value ($i \leq 10$), above which the rates drop off to a relatively lower but unified value. The nucleation rates obtained from YM method compared well with that from MFPT method, while being almost 4 orders of magnitude larger than the CNT steady-state value. The variations in the ensemble entropy of mixing indicated an increasing trend in the system leading up to the onset of nucleation where it eventually undergoes the expected drastic loss due to the emergence of a more organized new nanophase. This work paves the path for our future introduction of more accurate cluster size-dependent free energy formulations into our current nucleation model. Such a robust model development will facilitate the easy and unified incorporation of the nucleation process into our previously developed KMC-based collision-coalescence[42] and morphology-driven surface oxidation models[43] that can investigate the impact of nucleating critical cluster sizes on the general dynamics of NP growth and evolution without any capillarity and/or, isothermal assumptions.

Acknowledgments

The authors would like to thank one of the reviewers and Prof. Bamin Khomami (Chemical & Biomolecular Engineering Department, UTK) for providing valuable insights, comments, and discussions in regards to the calculation of the Gibbs' entropy of mixing in the manuscript.

Literature Cited

1. Park K, Lee D, Rai A, Mukherjee D, Zachariah MR. Size-resolved kinetic measurements of aluminum nanoparticle oxidation with single particle mass spectrometry. *J Phys Chem B*. 2005;109(15):7290–7299.
2. Rao CNR, Kulkarni GU, Thomas PJ, Edwards PP. Metal nanoparticles and their assemblies. *Chem Soc Rev*. 2000;29(1):27–35.
3. Prakash A, Bapat AP, Zachariah MR. A simple numerical algorithm and software for solution of nucleation, surface growth, and coagulation problems. *Aerosol Sci Technol*. 2003;37(11):892–898.
4. Mukherjee D, Davari SA. Computational modeling of fate, transport and evolution of energetic metal nanoparticles grown via aerosol route. In: Shukla M, Jeffery Steevens VB, Reddy D, Leszczynski J, editor. *Energetic Materials: from Cradle to Grave*, New York, USA: Springer, 2017.
5. Oxtoby DW. Homogeneous nucleation - theory and experiment. *J Phys-Condens Mat*. 1992;4(38):7627–7650.
6. Laaksonen A, Talanquer V, Oxtoby DW. Nucleation - measurements, theory, and atmospheric applications. *Ann Rev Phys Chem*. 1995;46:489–524.
7. Li ZH, Bhatt D, Schultz NE, Siepmann JI, Truhlar DG. Free energies of formation of metal clusters and nanoparticles from molecular simulations: Al-n with n=2–60. *J Phys Chem C*. 2007;111(44):16227–16242.
8. Girshick SL, Agarwal P, Truhlar DG. Homogeneous nucleation with magic numbers: aluminum. *J Chem Phys*. 2009;131(13):
9. Widiyastuti W, Purwanto A, Wang W-N, Iskandar F, Setyawan H, Okuyama K. Nanoparticle formation through solid-fed flame synthesis: experiment and modeling. *AIChE J*. 2009;55(4):885–895.
10. Mueller R, Jossen R, Kammler HK, Pratsinis SE, Akhtar MK. Growth of zirconia particles made by flame spray pyrolysis. *AIChE J*. 2004;50(12):3085–3094.
11. Mädler L, Kammler HK, Mueller R, Pratsinis SE. Controlled synthesis of nanostructured particles by flame spray pyrolysis. *J Aerosol Sci*. 2002;33(2):369–389.
12. Auer S, Frenkel D. Prediction of absolute crystal-nucleation rate in hard-sphere colloids. *Nature*. 2001;409(6823):1020–1023.
13. Valeriani C, Allen RJ, Morelli MJ, Frenkel D, ten Wolde PR. Computing stationary distributions in equilibrium and nonequilibrium systems with forward flux sampling. *J Chem Phys*. 2007;127:114109–114120.
14. Allen RJ, Valeriani C, ten Wolde PR. Forward flux sampling for rare event simulations. *J Phys-Condens Mat*. 2009;21:463102–463123.
15. Finney EE, Finke RG. Nanocluster nucleation and growth kinetic and mechanistic studies: a review emphasizing transition-metal nanoclusters. *J Colloid Interface Sci*. 2008;317(2):351–374.
16. Girshick SL, Chiu CP. Homogeneous nucleation of particles from the vapor-phase in thermal plasma synthesis. *Plasma Chem Plasma*. 1989;9(3):355–369.
17. Rusyniak M, Abdelsayed V, Campbell J, El-Shall MS. Vapor phase homogeneous nucleation of higher alkanes: dodecane, hexadecane, and octadecane. 1. Critical supersaturation and nucleation rate measurements†. *J Phys Chem B*. 2001;105(47):11866–11872.
18. Katz JL, Mirabel P, Scoppa CJ, Virkler TL. Condensation of a supersaturated vapor.3. Homogeneous nucleation of Ccl4, Chcl3, Ccl3f, and C2h2cl4. *J Chem Phys*. 1976;65(1):382–392.
19. Katz JL. Condensation of a supersaturated vapor.1. Homogeneous nucleation of normal-alkanes. *J Chem Phys*. 1970;52(9):4733.
20. McClurg RB, Flagan RC, Goddard WA. Thermodynamic properties and homogeneous nucleation for surface-melted physical clusters. *J Chem Phys*. 1996;105(17):7648–7663.
21. McClurg RB, Flagan RC. Critical comparison of droplet models in homogeneous nucleation theory. *J Colloid Interf Sci*. 1998;201(2):194–199.
22. Mukherjee D, Prakash A, Zachariah MR. Implementation of a discrete nodal model to probe the effect of size-dependent surface tension on nanoparticle formation and growth. *J Aerosol Sci*. 2006;37(10):1388–1399.
23. Palmer JC, Debenedetti PG. Recent advances in molecular simulation: a chemical engineering perspective. *AIChE J*. 2015;61(2):370–383.
24. Li ZH, Truhlar DG. Cluster and nanoparticle condensation and evaporation reactions. Thermal rate constants and equilibrium constants of Al(m)+Al(n-m)<-> Al(n) with n=2–60 and m=1–8. *J Phys Chem C*. 2008;112(30):11109–11121.
25. Panda S, Pratsinis SE. Modeling the synthesis of aluminum particles by evaporation-condensation in an aerosol flow reactor. *Nanostruct Mater*. 1995;5(7–8):755–767.
26. Shizgal B, Barrett JC. Time-dependent nucleation. *J Chem Phys*. 1989;91(10):6505–6518.
27. Roemer F, Braun S, Kraska T. Development of an EAM potential for zinc and its application to the growth of nanoparticles. *Phys Chem Chem Phys*. 2009;11(20):4039–4050.
28. Gillespie DT. Exact method for numerically simulating stochastic coalescence process in a cloud. *J Atmos Sci*. 1975;32(10):1977–1989.
29. Shah BH, Ramkrishna D, Borwanker JD. Simulation of particulate systems using concept of interval of quiescence. *AIChE J*. 1977;23(6):897–904.
30. Spouge JL. Monte-Carlo results for random coagulation. *J Colloid Interf Sci*. 1985;107(1):38–43.
31. Tandon P, Rosner DE. Monte Carlo simulation of particle aggregation and simultaneous restructuring. *J Colloid Interface Sci*. 1999;213(2):273–286.
32. Kruis FE, Maisels A, Fissan H. Direct simulation Monte Carlo method for particle coagulation and aggregation. *AIChE J*. 2000;46(9):1735–1742.
33. Efendiev Y, Zachariah MR. Hierarchical hybrid Monte-Carlo method for simulation of two-component aerosol nucleation, coagulation and phase segregation. *J Aerosol Sci*. 2003;34(2):169–188.
34. Khalili S, Lin YL, Armaou A, Matsoukas T. Constant number Monte Carlo simulation of population balances with multiple growth mechanisms. *AIChE J*. 2010;56(12):3137–3145.
35. Hao XM, Zhao HB, Xu ZW, Zheng CG. Population balance-Monte Carlo simulation for gas-to-particle synthesis of nanoparticles. *Aerosol Sci Technol*. 2013;47(10):1125–1133.
36. Zhao H, Kruis FE, Zheng C. Reducing statistical noise and extending the size spectrum by applying weighted simulation particles in Monte Carlo simulation of coagulation. *Aerosol Sci Tech*. 2009;43(8):781–793.
37. Zhao H, Kruis FE, Zheng C. A differentially weighted Monte Carlo method for two-component coagulation. *J Comput Phys*. 2010;229(19):6931–6945.
38. Liffman K. A direct simulation Monte-Carlo method for cluster coagulation. *J Comput Phys*. 1992;100(1):116–127.
39. Maisels A, Kruis FE, Fissan H. Direct simulation Monte Carlo for simultaneous nucleation, coagulation, and surface growth in dispersed systems. *Chem Eng Sci*. 2004;59(11):2231–2239.
40. Mukherjee D, Sonwane CG, Zachariah MR. Kinetic Monte Carlo simulation of the effect of coalescence energy release on the size and shape evolution of nanoparticles grown as an aerosol. *J Chem Phys*. 2003;119(6):3391–3404.
41. Smith M, Matsoukas T. Constant-number Monte Carlo simulation of population balances. *Chem Eng Sci*. 1998;53(9):1777–1786.
42. Bahadur R, McClurg RB. Comparison of cluster definitions in homogeneous nucleation rate calculations. *J Phys Chem B*. 2001;105(47):11893–11900.
43. Mukherjee D, Wang M, Khomami B. Impact of particle morphology on surface oxidation of nanoparticles: a kinetic Monte Carlo based study. *AIChE J*. 2012;58(11):3341–3353.
44. Efendiev Y, Zachariah MR. Hybrid Monte Carlo method for simulation of two-component aerosol coagulation and phase segregation. *J Colloid Interface Sci*. 2002;249(1):30–43.
45. Chkonia G, Wolk J, Strey R, Wedekind J, Reguera D. Evaluating nucleation rates in direct simulations. *J Chem Phys*. 2009;130:064505–064511.
46. Reddy VS, Karak S, Ray SK, Dhar A. Carrier transport mechanism in aluminum nanoparticle embedded AlQ(3) structures for organic bistable memory devices. *Org Electron*. 2009;10(1):138–144.
47. Zhong XL, Wong WLE, Gupta M. Enhancing strength and ductility of magnesium by integrating it with aluminum nanoparticles. *Acta Mater*. 2007;55(18):6338–6344.
48. Liang G, Tjong SC. Electrical conducting behavior of polyethylene composites filled with self-passivated aluminum nanoparticles and carbon nanotubes. *Adv Eng Mater*. 2007;9(11):1014–1017.
49. Tepper F, Ivanov GV. 'Activated' aluminum as a stored energy source for propellants. *Int J Energetic Mater Chem Propul*. 1997, 4(1–6):636–645.

50. Mukherjee D, Rai A, Zachariah MR. Quantitative laser-induced breakdown spectroscopy for aerosols via internal calibration: application to the oxidative coating of aluminum nanoparticles. *J Aerosol Sci*. 2006;37(6):677–695.
51. Sun J, Pantoya ML, Simon SL. Dependence of size and size distribution on reactivity of aluminum nanoparticles in reactions with oxygen and MoO3. *Thermochimica Acta*. 2006;444(2):117–127.
52. Trunov MA, Umbrajkar SM, Schoenitz M, Mang JT, Dreizin EL. Oxidation and melting of aluminum nanopowders. *J Phys Chem B*. 2006;110(26):13094–13099.
53. Russo MF, Li R, Mench M, van Duin ACT. Molecular dynamic simulation of aluminum-water reactions using the ReaxFF reactive force field. *Int J Hydrogen Energy*. 2011;36(10):5828–5835.
54. Vashishta P, Kalia RK, Nakano A. Multimillion atom simulations of dynamics of oxidation of an aluminum nanoparticle and nanoindentation on ceramics. *J Phys Chem B*. 2006;110(8):3727–3733.
55. Rai A, Park K, Zhou L, Zachariah MR. Understanding the mechanism of aluminium nanoparticle oxidation. *Combustion Theory Model*. 2006;10(5):843–859.
56. Huang Y, Risha GA, Yang V, Yetter RA. Effect of particle size on combustion of aluminum particle dust in air. *Combustion Flame*. 2009;156(1):5–13.
57. Yasuoka K, Matsumoto M. Molecular dynamics of homogeneous nucleation in the vapor phase. I. Lennard-Jones fluid. *J Chem Phys*. 1998;109(19):8451–8462.
58. Julin J, Napari I, Vehkamaki H. Comparative study on methodology in molecular dynamics simulation of nucleation. *J Chem Phys*. 2007; 126:224517–224525.
59. Wedekind J, Strey R, Reguera D. New method to analyze simulations of activated processes. *J Chem Phys*. 2007;126:134103–134110.
60. Wedekind J, Wolk J, Reguera D, Strey R. Nucleation rate isotherms of argon from molecular dynamics simulations. *J Chem Phys*. 2007; 127:154515–154526.
61. Romer F, Kraska T. Homogeneous nucleation and growth in supersaturated zinc vapor investigated by molecular dynamics simulation. *J Chem Phys*. 2007;127(23):127.

Manuscript received Feb. 19, 2017, and revision received July 10, 2017.